

# A Ring of C<sub>2</sub>H in the Molecular Disk Orbiting TW Hya

Joel H. Kastner<sup>1</sup>, Chunhua Qi<sup>2</sup>, Uma Gorti<sup>3</sup>, Pierre Hily-Blant<sup>4,5</sup>, Karin Oberg<sup>2</sup>, Thierry Forveille<sup>4</sup>, Sean Andrews<sup>2</sup>, David Wilner<sup>2</sup>

## ABSTRACT

We have used the Submillimeter Array to image, at  $\sim 1.5''$  resolution, C<sub>2</sub>H  $N = 3 \rightarrow 2$  emission from the circumstellar disk orbiting the nearby ( $D = 54$  pc),  $\sim 8$  Myr-old,  $\sim 0.8 M_{\odot}$  classical T Tauri star TW Hya. The SMA imaging reveals that the C<sub>2</sub>H emission exhibits a ring-like morphology. Based on a model in which the C<sub>2</sub>H column density follows a truncated radial power-law distribution, we find that the inner edge of the ring lies at  $\sim 45$  AU, and that the ring extends to at least  $\sim 120$  AU. Comparison with previous (single-dish) observations of C<sub>2</sub>H  $N = 4 \rightarrow 3$  emission indicates that the C<sub>2</sub>H molecules are subthermally excited and, hence, that the emission arises from the relatively warm ( $T \gtrsim 40$  K), tenuous ( $n \ll 10^7 \text{ cm}^{-3}$ ) upper atmosphere of the disk. Based on these results and comparisons of the SMA C<sub>2</sub>H map with previous submm and scattered-light imaging, we propose that the C<sub>2</sub>H emission most likely traces particularly efficient photo-destruction of small grains and/or photodesorption and photodissociation of hydrocarbons derived from grain ice mantles in the surface layers of the outer disk. The presence of a C<sub>2</sub>H ring in the TW Hya disk hence likely serves as a marker of dust grain processing and radial and vertical grain size segregation within the disk.

---

<sup>1</sup>Chester F. Carlson Center for Imaging Science, School of Physics & Astronomy, and Laboratory for Multiwavelength Astrophysics, Rochester Institute of Technology, 54 Lomb Memorial Drive, Rochester NY 14623 USA (jkh@cis.rit.edu)

<sup>2</sup>Harvard-Smithsonian Center for Astrophysics, 60 Garden Street, Cambridge, MA 02138

<sup>3</sup>SETI Institute, 189 Bernardo Ave., Mountain View, CA 94043, USA; NASA Ames Research Center, Moffett Field, CA 94035, USA

<sup>4</sup>Université Grenoble Alpes, Institut de Planétologie et d'Astrophysique de Grenoble (IPAG), F-38000, Grenoble, France; CNRS, IPAG, F-38000, Grenoble, France

<sup>5</sup>Institut Universitaire de France, F-38000, Grenoble, France

## 1. Introduction

Models of protoplanetary disks orbiting low-mass, pre-main sequence (T Tauri) stars predict that gas-grain processes and high-energy stellar irradiation are important ingredients in determining disk chemical composition and dust grain evolution (Walsh et al. 2014; Dutrey et al. 2014, and refs. therein). These evolutionary processes, in turn, have profound implications for planet-building scenarios, since disk dust and gas characteristics — such as characteristic dust grain sizes, the presence or absence of grain ice mantles, and gas-phase molecular abundances — should regulate the rate of planetesimal buildup and the compositions of bodies ranging from comets to giant planet envelopes (e.g., Dutrey et al. 2014, and refs. therein).

Interferometric imaging of molecule-rich disks orbiting nearby T Tauri star/disk systems — whose archetype is TW Hya ( $D = 54$  pc, age  $\sim 8$  Myr; Torres et al. 2008; Ducourant et al. 2014) — provides key insight into these and other planet formation processes (e.g., Qi et al. 2004, 2008; Hughes et al. 2011; Rosenfeld et al. 2012; Andrews et al. 2012). Recently, for example, imaging with the Atacama Large Millimeter Array (ALMA) established that  $\text{N}_2\text{H}^+$  emission from the TW Hya disk displays a central hole of radius  $\sim 30$  AU (Qi et al. 2013b). On the basis of simple gas-phase chemistry, Qi et al. (2013b) interpreted the  $\sim 30$  AU outer edge of the  $\text{N}_2\text{H}^+$  depletion region as tracing the CO “snow line,” i.e., the innermost radius at which CO freezes out onto dust grains.

In an unbiased molecular line survey of TW Hya spanning the wavelength range 0.85–1.1 mm, carried out with the Atacama Pathfinder Experiment (APEX) 12 m telescope, we detected strong  $\text{C}_2\text{H}$   $N = 4 \rightarrow 3$  emission (Kastner et al. 2014). From analysis of the hyperfine splitting of this transition, we determined that the emission is optically thick and either arises from very cold disk layers or is subthermally excited. We furthermore determined a very large beam-averaged  $\text{C}_2\text{H}$  column density of  $\sim 5 \times 10^{15} \text{ cm}^{-2}$ , suggesting that, in specific regions of the outer disk, the abundance of  $\text{C}_2\text{H}$  in the gas phase may rival or perhaps exceed that of CO. As  $\text{C}_2\text{H}$  is potentially a product of the photodissociation of more complex hydrocarbons and dissociative recombinations of molecular ions with electrons, its radio emission may trace the influence of stellar irradiation on molecular, protoplanetary disks (Henning et al. 2010; Walsh et al. 2010). To ascertain the surface brightness distribution of  $\text{C}_2\text{H}$  in the TW Hya disk, which is viewed nearly pole-on ( $i \approx 6^\circ$ , assuming a central star mass of  $\sim 0.8 M_\odot$ ; Qi et al. 2004; Andrews et al. 2012), we have carried out imaging of  $\text{C}_2\text{H}$   $N = 3 \rightarrow 2$  emission of TW Hya with the Submillimeter Array (SMA).

## 2. Observations and Data Reduction

Observations of 262 GHz  $\text{C}_2\text{H}$   $N = 3 \rightarrow 2$  emission and adjacent continuum centered at the position of TW Hya were obtained on 2013 April 5 and 2014 April 8 in the SMA’s compact (C) and extended (E) array configurations, respectively, with projected baselines ranging from 6.3 m to 164.8 m. The correlator setup included the four brightest hyperfine structure transitions of the  $\text{C}_2\text{H}$   $N = 3 \rightarrow 2$  rotational transition (which lie in the 262.004–262.067 GHz region; Table 1). The  $3_{3,3} - 2_{2,2}$  and  $3_{3,2} - 2_{2,1}$  transitions were observed in lower sideband correlator 104 MHz chunk S01, and were blended due to the coarse spectral resolution of  $1.86 \text{ km s}^{-1}$ , while the  $3_{4,4} - 3_{3,3}$  and  $3_{4,3} - 3_{3,2}$  transitions were observed in lower sideband correlator 104 MHz chunk S02 with spectral resolutions of  $0.46 \text{ km s}^{-1}$  (C) and  $0.23 \text{ km s}^{-1}$  (E), which resolves the two lines (Fig. 1, bottom panel). The observing loops used J1037–295 as the gain calibrator, and the bandpass response was calibrated using observations of 3C279. Flux calibration was performed using observations of Titan and Callisto. The derived fluxes of J1037–295 were 0.79 Jy on 2013 April 5 and 0.70 Jy on 2014 April 8. All data were phase- and amplitude-calibrated with the MIR software package<sup>1</sup>. Continuum and spectral line maps were then generated and CLEANed using the MIRIAD software package.

## 3. Results and Analysis

In Fig. 1, we display continuum (266 GHz) and  $\text{C}_2\text{H}$  emission line maps for the spectral region encompassing the  $3_{4,4} - 2_{3,3}$  and  $3_{4,3} - 2_{3,2}$  transitions of  $\text{C}_2\text{H}$ . From the merged (C+E) data, we measure a 266 GHz continuum flux of  $737 \pm 3 \text{ mJy}$  (averaged over both upper and lower sidebands) and integrated intensities of  $3.74$  and  $3.25 \text{ Jy km s}^{-1}$  ( $\pm 0.06 \text{ Jy km s}^{-1}$ ), respectively, for the  $3_{4,4} - 2_{3,3}$  and  $3_{4,3} - 2_{3,2}$  transitions (with absolute calibration uncertainties of  $\sim 10\%$ ). These total flux measurements likely account for all of the 266 GHz continuum flux and  $\text{C}_2\text{H}$   $N = 3 \rightarrow 2$  line emission from the TW Hya disk, given the angular scales probed by the shortest ( $\sim 6 \text{ m}$ ) SMA baselines at this frequency (e.g., Wilner & Welch 1994). The  $\text{C}_2\text{H}$  emission is evidently well resolved in the merged C+E configuration data (top row of Fig. 1). The E configuration map (lower middle panel of Fig. 1) reveals that the  $\text{C}_2\text{H}$  ( $3_{4,4} - 2_{3,3}$ ) emission has a ring-like morphology, with brightened limbs (ansae) in the E-W direction. In the  $\text{C}_2\text{H}$  ( $3_{4,3} - 2_{3,2}$ ) E configuration emission-line map (lower right panel), only the ansae are apparent.

---

<sup>1</sup><http://www.cfa.harvard.edu/~cqi/mircook.html>

The inner radius of the ring of  $\text{C}_2\text{H}$  ( $3_{4,4} - 2_{3,3}$ ) emission in the TW Hya disk, as imaged by the SMA, appears to be larger than that of the ring of  $\text{N}_2\text{H}^+$  ( $4-3$ ) emission as imaged by ALMA (Qi et al. 2013b). This comparison — which we further explore below (§3.2, 4.1) — suggests that despite their morphologically similar surface brightness distributions,  $\text{C}_2\text{H}$  and  $\text{N}_2\text{H}^+$  may trace different physical and/or chemical processes in the disk. The continuum emission is only marginally resolved in these maps, consistent with previous mm-wave interferometric imaging observations that established that the continuum emission from the TW Hya disk is quite compact relative to the disk molecular line emission (continuum and CO outer radii of  $\sim 60$  AU and  $\sim 200$  AU, respectively; e.g., Andrews et al. 2012).

### 3.1. Excitation of $\text{C}_2\text{H}$

Our analysis of the  $\text{C}_2\text{H}$   $N = 4 \rightarrow 3$  hyperfine emission complex had previously indicated that the  $\text{C}_2\text{H}$  emission either arises from very cold (midplane) disk layers, or that the  $\text{C}_2\text{H}$  molecules are subthermally excited (Kastner et al. 2014). The latter interpretation would suggest that the relative abundance of  $\text{C}_2\text{H}$  peaks high in the disk and, hence, is more consistent with the chemical simulations of protoplanetary disks presented by Walsh et al. (2010), in which the relative  $\text{C}_2\text{H}$  abundance peaks at relative heights  $z/R \sim 0.3$ .

To investigate whether and how the ratio of  $\text{C}_2\text{H}$   $N = 4 \rightarrow 3$  to  $N = 3 \rightarrow 2$  line intensities as measured with APEX ( $2.7 \text{ Jy km s}^{-1}$  for the 349.3375 GHz transition; Kastner et al. 2014) and SMA ( $3.74 \text{ Jy km s}^{-1}$  for the 262.0042 GHz transition; §3), respectively, constrains the physical conditions (hence height) of the layers of the disk from which the  $\text{C}_2\text{H}$  emission originates, we constructed a grid of models with the web-based RADEX tool<sup>2</sup> (van der Tak et al. 2007). RADEX calculates the emergent line flux under the local velocity gradient approximation, employing the same molecular data as used for the morphological analysis in §3.2. The resulting model  $\text{C}_2\text{H}$  ( $4-3$ )/( $3-2$ ) line ratios were then compared with the observed ratio, i.e.,  $(4-3)/(3-2) \approx 0.72$ . The results, which are illustrated in Fig. 2, indicate that the observed ( $4-3$ )/( $3-2$ ) line ratio can be reproduced in two specific regimes of physical conditions: (1)  $T \sim 15\text{--}25$  K and  $\log n > 7$ , or (2)  $T > 40$  K and  $\log n \sim 5\text{--}6$ . The latter conditions correspond to subthermal excitation of  $\text{C}_2\text{H}$ ; specifically, the critical densities for excitation of the  $3-2$  and  $4-3$  transitions of  $\text{C}_2\text{H}$  for a gas kinetic temperature  $T_k = 30$  K are  $n_{cr} \sim 0.6 \times 10^7 \text{ cm}^{-3}$  and  $\sim 2 \times 10^7 \text{ cm}^{-3}$  respectively (and the values of  $n_{cr}$  increase for smaller assumed values of  $T_k$ ).

In our tests of models that can reproduce the ring-like morphology of the  $\text{C}_2\text{H}$  emission

---

<sup>2</sup><http://www.sron.rug.nl/~vdtak/radex/index.shtml>

(§3.2), we find that models in which the  $\text{C}_2\text{H}$  is assumed to lie at relatively deep, dense layers of the disk consistently overpredict the observed  $(4-3)/(3-2)$  line ratio by a factor  $\sim 2$  or more, whereas models in which the  $\text{C}_2\text{H}$  lies high in the disk surface layers can reproduce the observed  $(4-3)/(3-2)$  line ratio to within  $\sim 30\%$ . Furthermore, the very low excitation temperature inferred from the  $\text{C}_2\text{H}$   $N = 4 \rightarrow 3$  modeling ( $T_{ex} \sim 6$  K; Kastner et al. 2014) is inconsistent with the observed  $(4-3)/(3-2)$  line ratio, under conditions of thermal excitation (Fig. 2). Hence, it appears that the  $\text{C}_2\text{H}$  is confined to low- $n$  (surface) disk layers, where it is subthermally excited.

### 3.2. Modeling the $\text{C}_2\text{H}$ emission morphology

To constrain the dimensions of the  $\text{C}_2\text{H}$  ring in the TW Hya disk, we modeled the SMA  $\text{C}_2\text{H}$  data via the same methodology used to analyze the ALMA  $\text{N}_2\text{H}^+$   $(4-3)$  data (Qi et al. 2013b). This methodology utilizes a model for the TW Hya disk (described in detail in Qi et al. 2004, 2006, 2013b) in which the non-local thermodynamic equilibrium, accelerated 2D Monte Carlo radiative transfer code RATRAN (Hogerheijde & van der Tak 2000) serves to calculate the molecular excitation. The data for the excitation calculations were drawn from Schöier et al. (2005), supplemented with  $\text{H}_2$  collisional rate coefficients from Spielfiedel et al. (2012) and electron impact rates appropriate for  $\text{C}_2\text{H}$  from A. Faure (2014, private comm.). As in the Qi et al. (2013b) treatment of  $\text{N}_2\text{H}^+$ , the  $\text{C}_2\text{H}$  emission is assumed to be produced within a vertical disk layer, of constant molecular abundance, whose boundaries are expressed in terms of vertically integrated hydrogen column densities as measured from the disk surface. The emitting molecular layer is confined to a ring with inner and outer edges  $R_{in}$  and  $R_{out}$ , respectively, with a column density that follows a power-law distribution, i.e.,  $N \propto R^p$ .

As noted earlier (§3.1), comparison of the SMA and APEX measurements indicates that the  $\text{C}_2\text{H}$  molecules are subthermally excited and, hence, reside in tenuous disk surface layers. In applying the foregoing ring-like molecular density distribution to model the TW Hya  $\text{C}_2\text{H}$  emission, we therefore focused on simulations in which the  $\text{C}_2\text{H}$  is confined to a thin surface layer. The specific models described here, which are representative of this family of simulations, have upper and lower vertical  $\text{C}_2\text{H}$  boundaries at  $\text{H}_2$  column densities of  $5 \times 10^{18} \text{ cm}^{-2}$  and  $8 \times 10^{18} \text{ cm}^{-2}$ , respectively.

With this vertical distribution fixed, we performed fits to the combined (C+E) visibilities for the resolved  $\text{C}_2\text{H}$  hyperfine lines, with the ring inner and outer ring edges  $R_{in}$ ,  $R_{out}$  and the density power-law index  $p$  left as free parameters. We find that the best-fit model, obtained by minimizing  $\chi^2$  for the weighted residuals in the visibilities, has  $R_{in} = 45 \text{ AU}$ ,

$R_{out} = 120$  AU, and  $p = -1.8$ . Based on a comparison of models with the foregoing values of  $R_{out}$  and  $p$  fixed but  $R_{in}$  allowed to vary, we find that only models with  $R_{in}$  in the range 40–50 AU well reproduce the observations (Fig. 3). The outer radius  $R_{out}$  is considerably less well constrained, due to degeneracy with the value of  $p$  during the model fitting (this degeneracy between  $R_{out}$  and  $p$  is a well-known aspect of power-law disk models; e.g., Mundy et al. 1996). We note that these results for the radial distribution of  $C_2H$  within the disk (i.e., the best-fit values for  $R_{out}$ ,  $R_{in}$ , and  $p$ ) are not sensitive to the assumed vertical placement of the layer from which the  $C_2H$  emission arises.

The distribution of  $C_2H$  in the best-fit surface layer model is shown schematically in Fig. 4. This distribution is qualitatively similar to that obtained in the simulations by Walsh et al. (2010), but lies at lower  $n$  (in our model, the  $C_2H$  emitting layer corresponds to a disk density  $n \approx 10^5$  cm $^{-3}$ ). The column density and approximate relative abundance of  $C_2H$  (with respect to  $H_2$ ) are  $N_{C_2H} = 8.4 \times 10^{14}$  cm $^{-2}$  and  $X_{C_2H} \sim 10^{-5}$ , respectively, near the inner emission boundary at  $R \approx 45$  AU and  $z \approx 20$  AU. The best-fit value of  $N_{C_2H}$  is similar to, though somewhat smaller than, that estimated from measurements of  $C_2H$  4–3 with APEX (Kastner et al. 2014). The value  $N_{C_2H} = 8.4 \times 10^{14}$  cm $^{-2}$  likely represents a lower limit on the  $C_2H$  column density at  $R \approx 45$  AU, given that the  $C_2H$  emitting layer could lie somewhat deeper in the disk without violating the constraints imposed by considerations of excitation (§3.1). The inferred value of  $X_{C_2H}$  suggests that the relative abundance of  $C_2H$  may rival that of CO in the gas phase, in this region of the disk (see, e.g., Qi et al. 2013b). The result for  $X_{C_2H}$  is highly uncertain, however, given that the model values of  $n$  and  $T$  are poorly constrained in the tenuous disk layers at high  $z/R$ , and that the precise  $C_2H$  emitting layer height and thickness is somewhat arbitrary.

## 4. Discussion

### 4.1. Radial distribution of $C_2H$

The modeling described in §3.1 (and illustrated in Fig 4) indicates that the inner edge of the  $C_2H$  ring imaged by the SMA,  $R_{in} \approx 45$  AU, lies roughly midway between the inner edge of  $N_2H^+$  emission as imaged by ALMA ( $\sim 30$  AU; Qi et al. 2013b) and the outer radius of submm continuum emission ( $\sim 60$  AU, as mapped at  $870 \mu m$  and  $806 \mu m$  with the SMA and ALMA, respectively; Andrews et al. 2012; Qi et al. 2013b). The  $N_2H^+$  emission inner cutoff likely traces the radius at which CO freezes out onto grain surfaces (Qi et al. 2013b), whereas the submm continuum outer cutoff marks the radius at which the large (radius  $\gtrsim 1$  mm) dust grain population drops precipitously. These two markers (at 30 AU and 60 AU) are well defined in the respective interferometric data, and neither disk radius is consistent

with the  $\text{C}_2\text{H}$  inner hole dimensions (Fig. 3). The location of the  $\text{C}_2\text{H}$  emission inner cutoff with respect to the CO snow line — and the persistence of  $\text{C}_2\text{H}$  emission at disk radii well beyond the drop in large-grain surface density — suggests that the  $\text{C}_2\text{H}$  abundance is enhanced in radial zones where small, ice-coated grains are plentiful. Indeed, at radii  $> 60$  AU, such small grains likely dominate the disk’s dust grain mass, based on the comparison between the aforementioned submm imaging and the extended ( $\sim 200$  AU radius) scattered-light “halo” seen in optical and near-infrared coronagraphic imaging with the *Hubble Space Telescope* (e.g., Debes et al. 2013, see §4.2.3).

## 4.2. $\text{C}_2\text{H}$ production mechanisms

In the following, we consider three potential processes that might enhance the abundance of  $\text{C}_2\text{H}$  in the surface layers of the TW Hya disk beyond  $\sim 45$  AU: *(i)* pure gas-phase production of  $\text{C}_2\text{H}$ , involving significant destruction of CO; *(ii)* X-ray photodesorption of organic ices on grains; and *(iii)* photodestruction of very small, C-rich grains and PAHs by UV and X-rays. As we describe below, mechanisms *(ii)* and *(iii)* may be acting in concert to produce the large inferred values of  $N_{\text{C}_2\text{H}}$ .

### 4.2.1. Gas-phase production

A large number of pure gas-phase processes could be responsible for production of  $\text{C}_2\text{H}$  (see, e.g., Fig. 7 in Henning et al. 2010). Many of these channels are initiated via destruction of CO and the consequent generation of ionized C (e.g., Aresu et al. 2011; Cleaves et al. 2013). Near the disk surface — above the layer where CO is photodissociated by stellar UV and X-ray photons — C ions and atoms can react with  $\text{H}_2$  and  $\text{CH}_3^+$ , respectively, to form  $\text{C}_2\text{H}_2^+$ , followed by recombination and dissociation to  $\text{C}_2\text{H}$ . This stellar-photon-driven process should produce a uniform (as opposed to ring-like)  $\text{C}_2\text{H}$  column density distribution over the disk surface, however, unless the  $\text{C}_2\text{H}$ -free region within  $\sim 45$  AU is shadowed from high-energy stellar irradiation by material in the inner disk (e.g., in a puffed-up inner rim at  $\sim 4$  AU; Andrews et al. 2012) .

In regions of the disk shielded from UV and X-rays, CR ionization of He results in the generation of free C. If the  $\text{C}_2\text{H}$  ring were generated via such a (CR-initiated) process, then it should be confined to the disk midplane, where high-energy CRs dominate the ionization rates (Cleaves et al. 2013). Indeed, our preliminary tests of pure gas-phase chemical models (utilizing a physical structure for the TW Hya disk described in detail in Gorti et al. 2011)

do yield a ring-like distribution of enhanced  $\text{C}_2\text{H}$ , with inner radius  $\sim 50$  AU, deep within the disk. However, this placement of the emitting  $\text{C}_2\text{H}$  (near the disk midplane) appears to be inconsistent with considerations of molecular excitation (§3.1). Furthermore, we find that these pure gas-phase models underpredict the  $\text{C}_2\text{H}$  column densities by at least an order of magnitude (similar modeling results were obtained by Henning et al. 2010). It therefore appears that pure gas-phase processes fail to explain the presence of the observed bright  $\text{C}_2\text{H}$  ring in the TW Hya disk.

#### 4.2.2. *X-ray photodesorption of organic ices*

In disk environments such as TW Hya’s, where primitive organics (e.g., CN, HCN and  $\text{C}_2\text{H}_2$ ) are relatively abundant (Kastner et al. 2014), it is likely that more complex organic molecules form and freeze out onto dust grains. Desorption of such ice-coated grains by stellar high-energy radiation — especially X-rays — can then be a rich source of dissociation products of the parent organics (Mendoza et al. 2013). It is not clear, however, whether an X-ray-dominated mechanism could produce  $\text{C}_2\text{H}$  high in the atmosphere of the outer disk, given that the stellar X-rays should penetrate relatively deeply within the disk (Cleeves et al. 2013). It is also possible that increasing gas/dust ratios in these more remote disk regions can facilitate the dredging of small, ice-coated grains to the disk surface, where they are efficiently irradiated by ice-destroying UV. However, this UV-driven photodesorption process should result in efficient  $\text{C}_2\text{H}$  production at radii  $< 45$  AU, i.e., at least to the CO “snow line” at  $\sim 30$  AU (see also Walsh et al. 2010). Hence — as in the case of pure gas-phase processes that are driven by stellar irradiation (§4.2.1) — “shadowing” of the disk outer regions (by inner disk material) might be required to explain the fact that the  $\text{C}_2\text{H}$  generated by ice photodesorption is evidently restricted to somewhat larger disk radii ( $\gtrsim 45$  AU).

#### 4.2.3. *Photodestruction of small grains and PAHs*

Dust grain fragmentation/coagulation equilibrium models (e.g., Birnstiel et al. 2011; Gorti et al. 2015) predict both a faster rate of grain growth in the inner disk, where gas densities are high, and more efficient collisional shattering of grains at large disk radii, where the gas surface densities are lower. The combination of the relatively sharp cutoff of submm emission in the TW Hya disk at  $\sim 60$  AU (Andrews et al. 2012) and the much larger extent of the disk in scattered near-infrared light (Debes et al. 2013) is consistent with such modeling. This contrast likely reflects a transition within the disk from efficient dust grain coagulation



and settling to more efficient grain fragmentation and levitation.

The outer disk environment hence may harbor an enhanced abundance of very small grains and polycyclic aromatic hydrocarbons (PAHs), particularly in the disk’s upper layers (see, e.g., Fig. 7 in Gorti et al. 2015). Once exposed to stellar UV and X-rays, these small grains and PAHs would undergo photodegradation to form loose  $\text{C}_2\text{H}_2$  groups (Allain et al. 1996), which would then photodissociate to produce the observed  $\text{C}_2\text{H}$ . Preliminary calculations, based on a simple scheme whereby UV irradiation breaks PAHs into  $\text{C}_2\text{H}_2$  units, suggest that to explain the  $\text{C}_2\text{H}$  column density inferred here (i.e.,  $N_{\text{C}_2\text{H}} \sim 10^{15} \text{ cm}^{-2}$ ), the relative abundance of PAHs per H nucleus in the upper layers of the disk would need to be perhaps an order of magnitude larger than the canonical relative PAH abundance in the interstellar medium ( $\sim 8 \times 10^{-7}$ ; Tielens 2008). As noted, such an enhanced PAH abundance could be a byproduct of the steeply falling gas surface density in the outer disk, which should yield disk conditions favorable for the production of small grains. Furthermore, inclusion of X-rays in the PAH photodestruction model would lower the required PAH abundance. Hence, in light of the modeling results presented in (§3.1, 3.2), we consider photodestruction of small grains and PAHs in disk surface layers to be a plausible source of the observed  $\text{C}_2\text{H}$ . The  $\text{C}_2\text{H}$  production rates from irradiated small grains would be further enhanced if organic ices coat these grains (§4.2.2).

### 4.3. Origin of the $\text{C}_2\text{H}$ ring

We propose the following schematic model to explain the  $\text{C}_2\text{H}$  spatial distribution, and its apparently subthermal excitation, within the TW Hya disk. Large surface densities are required to form submm-sized grains, which also drift radially as the disk evolves; such grain growth and migration manifests itself as a sharp edge in the submm dust grain distribution (Andrews et al. 2012). A corresponding increase in small grain surface density in the disk upper layers moving radially outward, evidently beginning at radii as small as  $\sim 45 \text{ AU}$ , then provides “fertile ground” for UV and soft X-rays generated at TW Hya (via chromospheric activity and accretion shocks; e.g., Kastner et al. 2002) to efficiently destroy small grains, PAHs, and/or grain mantles composed of organic ices. These photodestruction and photodesorption processes generate hydrocarbons (predominantly  $\text{C}_2\text{H}_2$ ) and, via subsequent photodissociations,  $\text{C}_2\text{H}$ . Although pure gas-phase reactions (catalyzed by high-energy stellar irradiation) could also be responsible for  $\text{C}_2\text{H}$  production, it is unclear whether such processes could produce the observed ring-like  $\text{C}_2\text{H}$  morphology at the large abundances and low densities inferred from the data.

Additional observations and modeling of  $\text{C}_2\text{H}$  emission from other, nearby protoplan-

tary disks are necessary to test and expand on the mechanisms proposed here to explain the spatial distribution and production of  $\text{C}_2\text{H}$  in the TW Hya disk. Indeed, few radio measurements of  $\text{C}_2\text{H}$  toward disks, either interferometric or single-dish, have been published thus far, and the scant interferometric data that do exist (e.g., Henning et al. 2010) are not of sufficient quality to determine disk  $\text{C}_2\text{H}$  emission morphologies. The results of our recent single-dish line surveys of V4046 Sgr (Kastner et al. 2014) and LkCa 15 (Punzi et al. 2015) indicate that these two disks are particularly deserving of followup interferometric imaging in  $\text{C}_2\text{H}$ . In each case, the inferred  $\text{C}_2\text{H}$  abundance and excitation is similar to that of TW Hya, indicating that both disks may also display ring-like  $\text{C}_2\text{H}$  surface brightness distributions.

We further note that in PAH-rich, UV-irradiated environments such as the Orion Bar,  $\text{C}_2\text{H}$  is merely the most abundant of a series of gas-phase hydrocarbons that are potentially detectable in the submm, including  $\text{C}_4\text{H}$ ,  $\text{c-C}_3\text{H}_2$ , and  $\text{c-C}_3\text{H}$ , among others (e.g., Cuadrado et al. 2015). Of these, only  $\text{c-C}_3\text{H}_2$  has thus far been detected in a circumstellar molecular disk (HD 163296; Qi et al. 2013a). Sensitive searches for this molecule and other simple hydrocarbons are warranted for TW Hya and the other two disks just mentioned, to further test the various  $\text{C}_2$  production scenarios proposed in §4.2.

## 5. Conclusions

The SMA imaging reported here reveals that  $\text{C}_2\text{H}(3-2)$  emission from the TW Hya disk exhibits a ring-like morphology with inner and outer radii of  $\sim 1''$  and  $\sim 3''$ , respectively. Radiative transfer modeling indicates that the inner edge of the  $\text{C}_2\text{H}$  ring lies at  $\sim 45$  AU and that the ring extends to at least  $\sim 120$  AU; we estimate a lower limit on the  $\text{C}_2\text{H}$  column density of  $N_{\text{C}_2\text{H}} \sim 10^{15} \text{ cm}^{-2}$  near the inner edge of the ring. The inferred inner cutoff of the  $\text{C}_2\text{H}$  emission lies roughly midway between the CO “snow line” at  $\sim 30$  AU (as inferred from  $\text{N}_2\text{H}^+$  emission line imaging) and the sharp decline in submm-sized dust grains at  $\sim 60$  AU (as inferred from submm continuum emission). Comparison with single-dish observations of  $\text{C}_2\text{H}(4-3)$  suggests that the  $\text{C}_2\text{H}$  emission emanates from tenuous upper layers of the disk (characterized by disk heights  $z/R \sim 0.5$  and gas densities  $n \ll 10^7 \text{ cm}^{-3}$ ), where the molecules are subthermally excited. While we cannot rule out the possibility that the  $\text{C}_2\text{H}$  arises in colder ( $T \sim 20$  K), higher-density regions of the disk, it is more difficult for such a model to explain the ensemble of observations obtained to date.

We propose that the  $\text{C}_2\text{H}$  emission most likely traces particularly efficient photo-destruction of small grains and/or photodesorption and photodissociation of hydrocarbons in the surface layers of the outer disk. The presence of a  $\text{C}_2\text{H}$  ring in the TW Hya disk therefore may be a byproduct of dust grain processing and migration, which is in turn associated with recent

or ongoing giant planet building interior to the ring. Given such a scenario, it remains to explain why the inner cutoff in  $\text{C}_2\text{H}$  at  $\sim 45$  AU evidently lies interior to the outer cutoff in the large grain surface density. These results hence stress the need for higher-resolution (i.e., ALMA) imaging to confirm and extend the results presented here for TW Hya, and to establish the radial and vertical distributions of  $\text{C}_2\text{H}$  within additional examples of nearby, evolved protoplanetary disks orbiting actively accreting T Tauri stars (e.g., V4046 Sgr, MP Mus, T Cha, LkCa 15; Sacco et al. 2014; Punzi et al. 2015).

*The Submillimeter Array is a joint project between the Smithsonian Astrophysical Observatory and the Academia Sinica Institute of Astronomy and Astrophysics and is funded by the Smithsonian Institution and the Academia Sinica. We gratefully acknowledge Alexander Faure for providing electron impact rates for  $\text{C}_2\text{H}$ , and we thank the anonymous referee for helpful comments and suggestions. This research is supported by National Science Foundation grant AST-1108950 to RIT and NASA Origins of Solar Systems grant NNX11AK63 to SAO.*

## REFERENCES

- Allain, T., Leach, S., & Sedlmayr, E. 1996, A&A, 305, 602
- Andrews, S. M., et al. 2012, ApJ, 744, 162
- Aresu, G., Kamp, I., Meijerink, R., Woitke, P., Thi, W.-F., & Spaans, M. 2011, A&A, 526, A163
- Birnstiel, T., Ormel, C. W., & Dullemond, C. P. 2011, A&A, 525, A11
- Cleeves, L. I., Adams, F. C., & Bergin, E. A. 2013, ApJ, 772, 5
- Cuadrado, S., Goicoechea, J. R., Pilleri, P., Cernicharo, J., Fuente, A., & Joblin, C. 2015, A&A, 575, A82
- Debes, J. H., Jang-Condell, H., Weinberger, A. J., Roberge, A., & Schneider, G. 2013, ApJ, 771, 45
- Ducourant, C., Teixeira, R., Galli, P. A. B., Le Campion, J. F., Krone-Martins, A., Zuckerman, B., Chauvin, G., & Song, I. 2014, A&A, 563, A121
- Dutrey, A., et al. 2014, Protostars and Planets VI, 317

- Gorti, U., Hollenbach, D., & Dullemond, C. 2015, ArXiv e-prints
- Gorti, U., Hollenbach, D., Najita, J., & Pascucci, I. 2011, *ApJ*, 735, 90
- Henning, T., et al. 2010, *ApJ*, 714, 1511
- Hogerheijde, M. R., & van der Tak, F. F. S. 2000, *A&A*, 362, 697
- Hughes, A. M., Wilner, D. J., Andrews, S. M., Qi, C., & Hogerheijde, M. R. 2011, *ApJ*, 727, 85
- Kastner, J. H., Hily-Blant, P., Rodriguez, D. R., Punzi, K., & Forveille, T. 2014, *ApJ*, 793, 55
- Kastner, J. H., Huenemoerder, D. P., Schulz, N. S., Canizares, C. R., & Weintraub, D. A. 2002, *ApJ*, 567, 434
- Mendoza, E., Almeida, G. C., Andrade, D. P. P., Luna, H., Wolff, W., Rocco, M. L. M., & Boechat-Roberty, H. M. 2013, *MNRAS*, 433, 3440
- Mundy, L. G., et al. 1996, *ApJ*, 464, L169
- Punzi, K., Hily-Blant, P., Kastner, J. H., Forveille, T., & Sacco, G. G. 2015, *ApJ*, submitted
- Qi, C., Öberg, K. I., Wilner, D. J., & Rosenfeld, K. A. 2013a, *ApJ*, 765, L14
- Qi, C., Wilner, D. J., Aikawa, Y., Blake, G. A., & Hogerheijde, M. R. 2008, *ApJ*, 681, 1396
- Qi, C., Wilner, D. J., Calvet, N., Bourke, T. L., Blake, G. A., Hogerheijde, M. R., Ho, P. T. P., & Bergin, E. 2006, *ApJ*, 636, L157
- Qi, C., et al. 2004, *ApJ*, 616, L11
- . 2013b, *Science*, 341, 630
- Rosenfeld, K. A., et al. 2012, *ApJ*, 757, 129
- Sacco, G. G., Kastner, J. H., Forveille, T., Principe, D., Montez, R., Zuckerman, B., & Hily-Blant, P. 2014, *A&A*, 561, A42
- Schöier, F. L., van der Tak, F. F. S., van Dishoeck, E. F., & Black, J. H. 2005, *A&A*, 432, 369
- Spielfiedel, A., Feautrier, N., Najar, F., Ben Abdallah, D., Dayou, F., Senent, M. L., & Lique, F. 2012, *MNRAS*, 421, 1891

- Tielens, A. G. G. M. 2008, *ARA&A*, 46, 289
- Torres, C. A. O., Quast, G. R., Melo, C. H. F., & Sterzik, M. F. 2008, *Young Nearby Loose Associations*, ed. Reipurth, B., 757–+
- van der Tak, F. F. S., Black, J. H., Schöier, F. L., Jansen, D. J., & van Dishoeck, E. F. 2007, *A&A*, 468, 627
- Walsh, C., Millar, T. J., & Nomura, H. 2010, *ApJ*, 722, 1607
- Walsh, C., Millar, T. J., Nomura, H., Herbst, E., Widicus Weaver, S., Aikawa, Y., Laas, J. C., & Vasyunin, A. I. 2014, *A&A*, 563, A33
- Wilner, D. J., & Welch, W. J. 1994, *ApJ*, 427, 898

Table 1: SMA CORRELATOR SETUPS FOR TW HYA C<sub>2</sub>H OBSERVATIONS

C <sub>2</sub> H transition	Frequency (GHz)	Resolution (km s <sup>-1</sup> )
$N = 3 \rightarrow 2, J = 7/2 \rightarrow 5/2, F = 4 \rightarrow 3$ ( $3_{4,4} - 3_{3,3}$ )	262.004266	0.46 (C), 0.23 (E)
$N = 3 \rightarrow 2, J = 7/2 \rightarrow 5/2, F = 3 \rightarrow 2$ ( $3_{4,3} - 3_{3,2}$ )	262.0064034	0.46 (C), 0.23 (E)
$N = 3 \rightarrow 2, J = 5/2 \rightarrow 3/2, F = 3 \rightarrow 2$ ( $3_{3,3} - 2_{2,2}$ )	262.0648433	1.86
$N = 3 \rightarrow 2, J = 5/2 \rightarrow 3/2, F = 2 \rightarrow 1$ ( $3_{3,2} - 2_{2,1}$ )	262.0673312	1.86

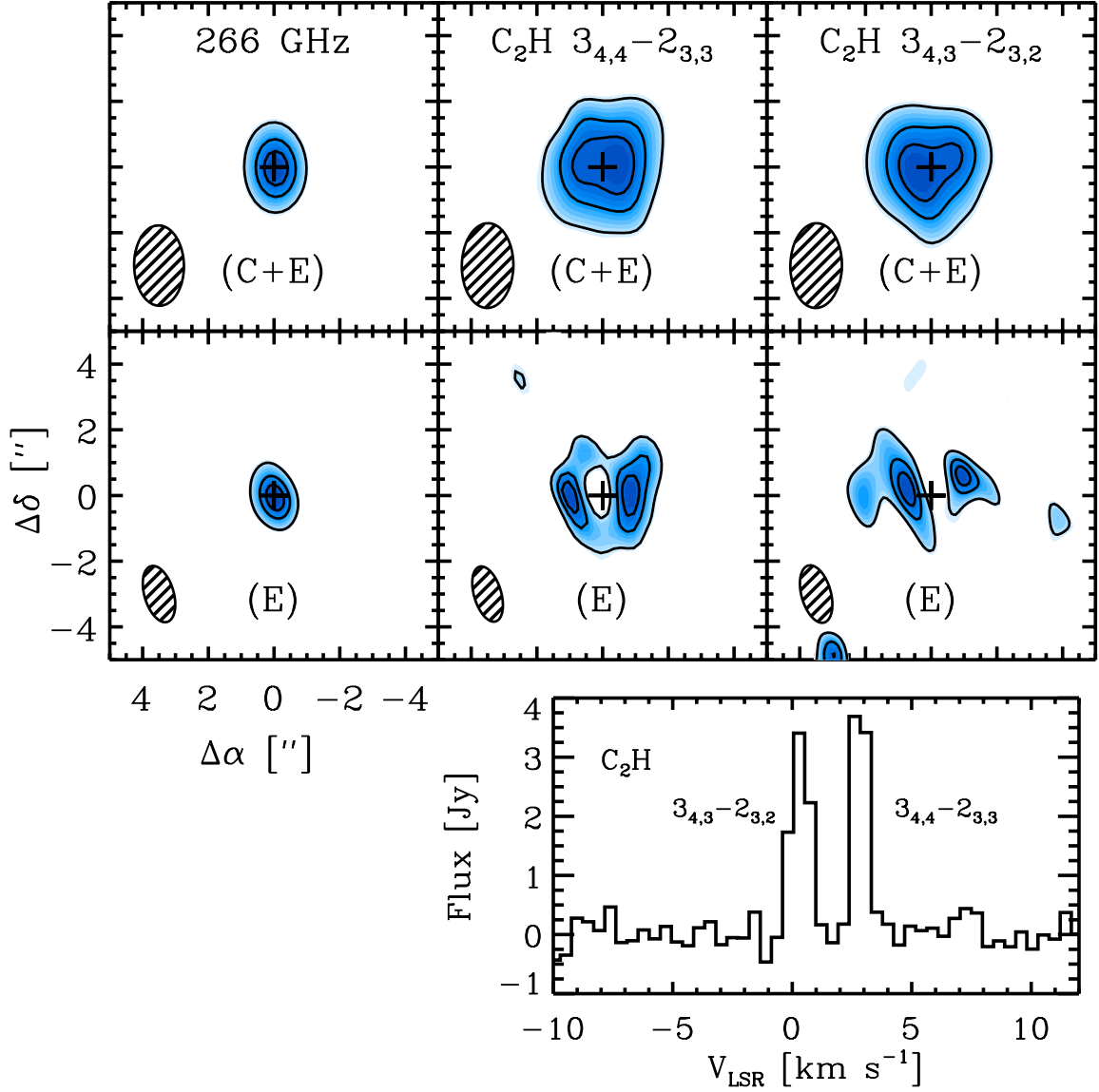


Fig. 1.— *Upper two rows of panels:* spectral line maps of the TW Hya disk in 266 GHz continuum (left) and  $\text{C}_2\text{H}$  (3–2) hyperfine lines (center and right) synthesized from data obtained in merged compact+extended (C+E; top panels) and extended (E; middle panels) SMA antenna configurations. In each panel, the shaded oval indicates the FWHM and orientation of the synthesized beams, and the cross represents the position of TW Hya (J2000 coordinates  $\alpha = 11:01:51.834$ ,  $\delta = -34:42:17.149$ ). Contours levels are 50%, 75% and 90% of the peak in each image. For the C+E (E) configurations, these peak fluxes are: 570 (401)  $\text{mJy beam}^{-1}$  for the 266 GHz continuum map, 1.33 (0.49)  $\text{Jy km s}^{-1} \text{beam}^{-1}$  for the  $3_{4,4} - 2_{3,3}$  transition map, and 1.18 (0.41)  $\text{Jy km s}^{-1} \text{beam}^{-1}$  for the  $3_{4,3} - 2_{3,2}$  transition map, with noise levels of 5 (8) and 0.04 (0.08) for the continuum and line maps, respectively. *Bottom panel:* spectrum of  $\text{C}_2\text{H}$  (3–2) hyperfine lines in the 262.005 GHz spectral region.

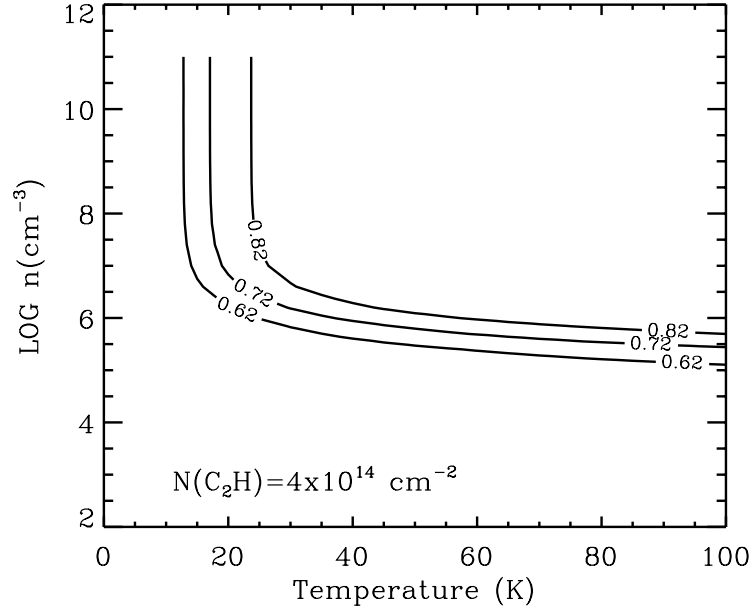


Fig. 2.— RADEX calculations of  $\text{C}_2\text{H}$  (4–3/3–2) ratios (see §3.1) as functions of disk  $\text{H}_2$  number density ( $n$ ) and gas kinetic temperature ( $T$ ) for an assumed  $\text{C}_2\text{H}$  column density of  $4 \times 10^{14} \text{ cm}^{-2}$  (corresponding to a radial position of  $\sim 60 \text{ AU}$ , in the surface layer model; §3.2) and linewidth  $0.7 \text{ km s}^{-1}$ . The contours indicate the values of  $n$  and  $T$  needed to match the observed  $\text{C}_2\text{H}$  (4–3/3–2) line ratio (0.72) and its approximate range of uncertainty ( $\sim \pm 0.1$ ).

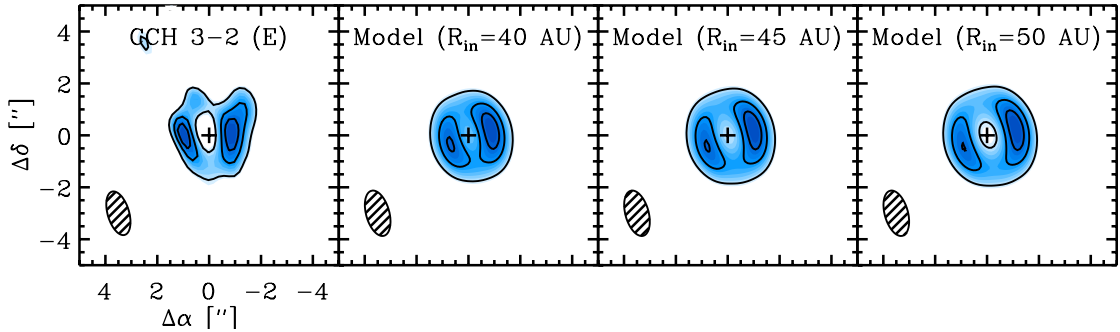


Fig. 3.— Comparison of observed (left panel) vs. model (remaining panels) maps of  $\text{C}_2\text{H}$  emission from the TW Hya disk. In each panel, the shaded oval indicates the FWHM and orientation of the synthesized or model beam, and the cross represents the position of the central star. The inner radii of the model  $\text{C}_2\text{H}$  rings are indicated in each panel. All models displayed here have the same (best-fit) values of outer radius (120 AU) and density power-law index ( $-1.8$ ).



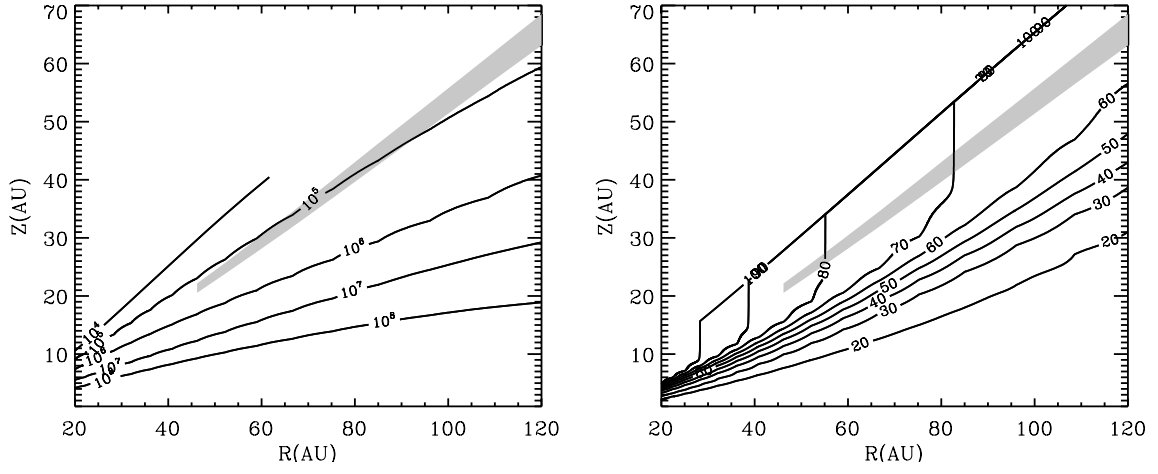


Fig. 4.— Distribution of  $\text{C}_2\text{H}$  for the best-fit model, overlaid as grey shading on contour plots of disk density (*left*, in  $\text{cm}^{-3}$ ) and gas kinetic temperature (*right*, in K).